

Long-range inputs and H-current regulate different modes of operation in a multiscale model of mouse M1 microcircuits

Salvador Dura-Bernal¹
 Samuel A Neymotin^{1,2}
 Benjamin A Suter³
 Gordon M G Shepherd⁴
 William W Lytton^{1,5}

¹ Dept. Physiology & Pharmacology, SUNY Downstate, Brooklyn, NY

² Brown University

³ IST Austria

⁴ Department of Physiology, Northwestern University

⁵ Dept. Neurology, Kings County Hospital Center, Brooklyn, NY

March 27, 2018

Abstract

We developed a biologically detailed multiscale model of mouse primary motor cortex (M1) microcircuits, incorporating data from several recent experimental studies. The model simulates at scale a cylindrical volume with a diameter of 300 μm and cortical depth 1350 μm of M1. It includes over 10,000 cells distributed across cortical layers based on measured cell densities, with close to 30 million synaptic connections. Neuron models were optimized to reproduce electrophysiological properties of major classes of M1 neurons. Layer 5 corticospinal and corticostriatal neuron morphologies with 700+ compartments reproduced cell 3D reconstructions, and their ionic channel distributions were optimized within experimental constraints to reproduce in vitro recordings. The network was driven by the main long-range inputs to M1: posterior nucleus (PO) and ventrolateral (VL) thalamus PO, primary and secondary somatosensory cortices (S1, S2), contralateral M1, secondary motor cortex (M2), and orbital cortex (OC). The network local and long-range connections depended on pre- and post-synaptic cell class and cortical depth. Data was based on optogenetic circuit mapping studies which determined that connection strengths vary within layer as a function of the neuron's cortical depth. The synaptic input distribution across cell dendritic trees – likely to subserve important neural coding functions – was also mapped using optogenetic methods and incorporated into the model. We employed the model to study the effect on M1 of increased activity from each of the long-range inputs, and of different levels of H-current in pyramidal tract-projecting (PT) corticospinal neurons. Microcircuit dynamics and information flow were quantified using firing rates, oscillations, and information transfer measures (Spectral Granger causality). We evaluated the response to short pulses and long time-varying activity arising from the different long-range inputs. We also studied the interaction between two simultaneous long-range inputs. Simulation results support the hypothesis that M1 operates along a continuum of modes characterized by the degree of activation of intratelencephalic (IT), corticothalamic (CT) and PT neurons. The particular subset of M1 neurons targeted by different long-range inputs and the level of H-current in PT neurons regulated the different modes. Downregulation of H-current facilitated synaptic integration of inputs and increased PT output activity. Therefore, VL, cM1 and M2 inputs with downregulated H-current promoted an PT-predominant mode; whereas PO, S1

and S2 inputs with upregulated H-current favored an IT-predominant mode, but a mixed mode where upper layer IT cells in turn activated PT cells if H-current was downregulated. This evidenced two different pathways that can generate corticospinal output: motor-related inputs bypassing upper M1 layers and directly projecting to PT cells, and sensory-related inputs projecting to superficial IT neurons in turn exciting PT cells. These findings provide a hypothetical mechanism to translate action planning into action execution. Overall, our model serves as an extensible framework to combine experimental data at multiple scales and perform in silico experiments that help us understand M1 microcircuit dynamics, information flow and biophysical mechanisms, and potentially develop treatments for motor disorders.

1 Introduction

Primary motor cortex (M1) microcircuits exhibit many differences with those of other cortices – *e.g.*, visual [59] – and with the traditional “canonical” microcircuit proposed by Douglas and Martin almost 30 years ago [12]. These include differences in the cytoarchitecture, cell classes and long and local connectivity. Notable characteristics that demarcate mouse M1 from sensory cortices are a narrower layer 4 and wider layer 5B [70], and its strongly asymmetrical projection: upper layer intratelencephalic (IT) cells connect to layer 5B pyramidal-tract (PT) cells but PT cells do not project back [68, 2]. Corticocortical and corticostriatal cells in superficial layers seem to play a role in recurrently processing information at a local level and within thalamocortical and striatal regions, whereas deep corticospinal cells output information (motor commands) from M1 to spinal cord circuits [52, 68, 2]. These distinctions have profound consequences in terms of understanding neural dynamics and information processing [58], and should therefore be considered when developing detailed biophysical models of M1.

We developed a detailed model of M1 microcircuits that combines data at multiple scales from multiple studies: including cell classes morphology, physiology, densities and proportions; and long-range, local, and dendritic-level connectivity. Most data was obtained from studies on the same species and region – mouse M1 – and combined into a single theoretical framework. To integrate all these experimental findings we developed several methodological novelties including specifying connections as a function of normalized cortical depth (NCD) instead of the standard layers, and incorporating projection-specific dendritic distributions of synaptic inputs extracted from subcellular Channelrhodopsin-2- Assisted Circuit Mapping (sCRACM) studies [21, 63]. Additionally, we developed a novel tool, NetPyNE, to help develop, simulate and analyze data-driven biological network models in NEURON [55] (www.netpyne.org).

Our model, which contains over 10 thousand neurons, 30 million synapses and models a cylindric cortical volume with a depth of 1350 μm and a diameter of 300 μm constitutes the most biophysically detailed model of mouse M1 microcircuits available. It enables studying the non-intuitive dynamics and interactions occurring across multiple scales, with a level of resolution and precision which is not yet available experimentally. Cortical circuits can have extremely disparate responses to changes in their cellular and subcellular properties; detailed simulation provides a means to systematically explore the circuit-level consequences of manipulations of the cellular components and wiring of the system.

In this study we explore the effect on M1 of increased activity from the different long-range inputs projecting into M1; and of regulation of H-current in PT corticospinal cells. We evaluate the hypothesis that different that M1 operates along a continuum of modes characterized by the level of activation of intratelencephalic (IT), corticothalamic (CT) and PT neurons, and that long-range inputs and H-current modulates which of these modes predominate. To do this, we first demonstrate our model exhibits spontaneous neural activity and oscillations consistent with M1 microcircuits. We then study its response to short pulses and long time-varying signals as inputs to S2 and M2, both independently and simultaneously, and with two different levels of PT H-current.

2 Methods

2.1 Morphology and physiology of neuron classes

Seven excitatory pyramidal cell and two interneuron cell models were employed in the network. Their morphology and physiological responses are summarized in Fig. 1.

In previous work we developed layer 5B PT corticospinal cell and L5 IT corticostriatal cell models that reproduce in vitro electrophysiological responses to somatic current injections, including sub- and super-threshold voltage trajectories and f-I curves [46, 62]. To achieve this we optimized the parameters of the Hodgkin-Huxley neuron model ionic channels – Na, Kdr, Ka, Kd, HCN, CaL, CaN, KCa – within a range of values constrained by literature. The corticospinal and corticostriatal cell model morphologies had 706 and 325 compartments, respectively, digitally reconstructed from 3D microscopy images. Morphologies are available via NeuroMorpho.org [?] (archive name “Suter_Shepherd”). We further improved the PT model by 1) increasing the concentration of Ca2+ channels (“hot zones”) between the nexus and apical tuft, following parameters published in [19]; 2) lowering dendritic Na+ channel density in order to increase the threshold required to elicit dendritic spikes, which then required adapting the axon sodium conductance and axial resistance to maintain a similar f-I curve; 3) replacing the HCN channel model and distribution with a more recent implementation by Migliore [43]. The new HCN channel reproduced a wider range of experimental observations than our previous implementation [29], including the change from excitatory to inhibitory effect in response to synaptic inputs of increasing strength [16]. This was achieved by including a shunting current proportional to I_h . We tuned the HCN parameters (lk and v_{revlk}) – originally developed for a CA3 pyramidal neuron [43] – and passive parameters to reproduce these experimental findings using the corticospinal cell, while keeping its somatic f-I curve consistent with recordings [62].

The network model includes five other excitatory cell classes: layer 2/3, layer 4, layer 5B and layer 6 IT neurons and layer 6 CT neurons. Since our focus was on the role of L5 neurons, other cell classes were implemented using simpler models as a trade-off to enable running a larger number of exploratory network simulations. Previously we had optimized 6-compartment neuron models to reproduce somatic current clamp recordings from two IT cells in layers 5A and 5B. The layer 5A cell had a lower f-I slope (X) and higher rheobase (X) than that in layer 5B (X and X). Based on our own and published data, we found two broad IT categories based on projection and intrinsic properties: corticocortical IT cells found in upper layers 2/3 and 4 which exhibited a lower f-I slope (avg X) and higher rheobase (avg X) than IT corticostriatal cells in deeper layers 5A, 5B and 6 (avg X and X) [70, 62, 49]. CT neurons’ f-I rheobase and slope (X and X) was closer to that of corticocortical neurons [49]. We therefore employed the layer 5A IT model for layers 2/3 and 4 IT neurons and layer 6 CT neurons, and the layer 5B IT model for layers 5A, 5B and 6 IT neurons. We further adapted cell models by modifying their apical dendrite length to match the average cortical depth of the layer, thus introducing small variations in the firing responses of neurons across layers.

We implemented models for two major classes of GABAergic interneurons [18]: parvalbumin-expressing fast-spiking (PV) and somatostatin-expressing low-threshold spiking neurons (SOM). We employed existing simplified 3-compartment (soma, axon, dendrite) models [30] and increased their dendritic length to better match the average f-I slope and rheobase experimental values of cortical basket (PV) and Martinotti (SOM) cells (Neuroelectro online database [64]).

2.2 Microcircuit composition: neuron locations, densities and ratios

We modeled in full scale a cylindric volume of mouse M1 cortical microcircuits with a 300 μm diameter and 1350 μm height (cortical depth) with a total of 10,171 neurons Fig. 1A. The cylinder diameter was chosen to approximately match the horizontal dendritic span of a corticospinal neuron located at the center, consistent with the approach used in the HBP model of rat S1 microcircuits [40]. Mouse cortical depth and boundaries for layers 2/3, 4, 5A, 5B and 6 were based on our published experimental data

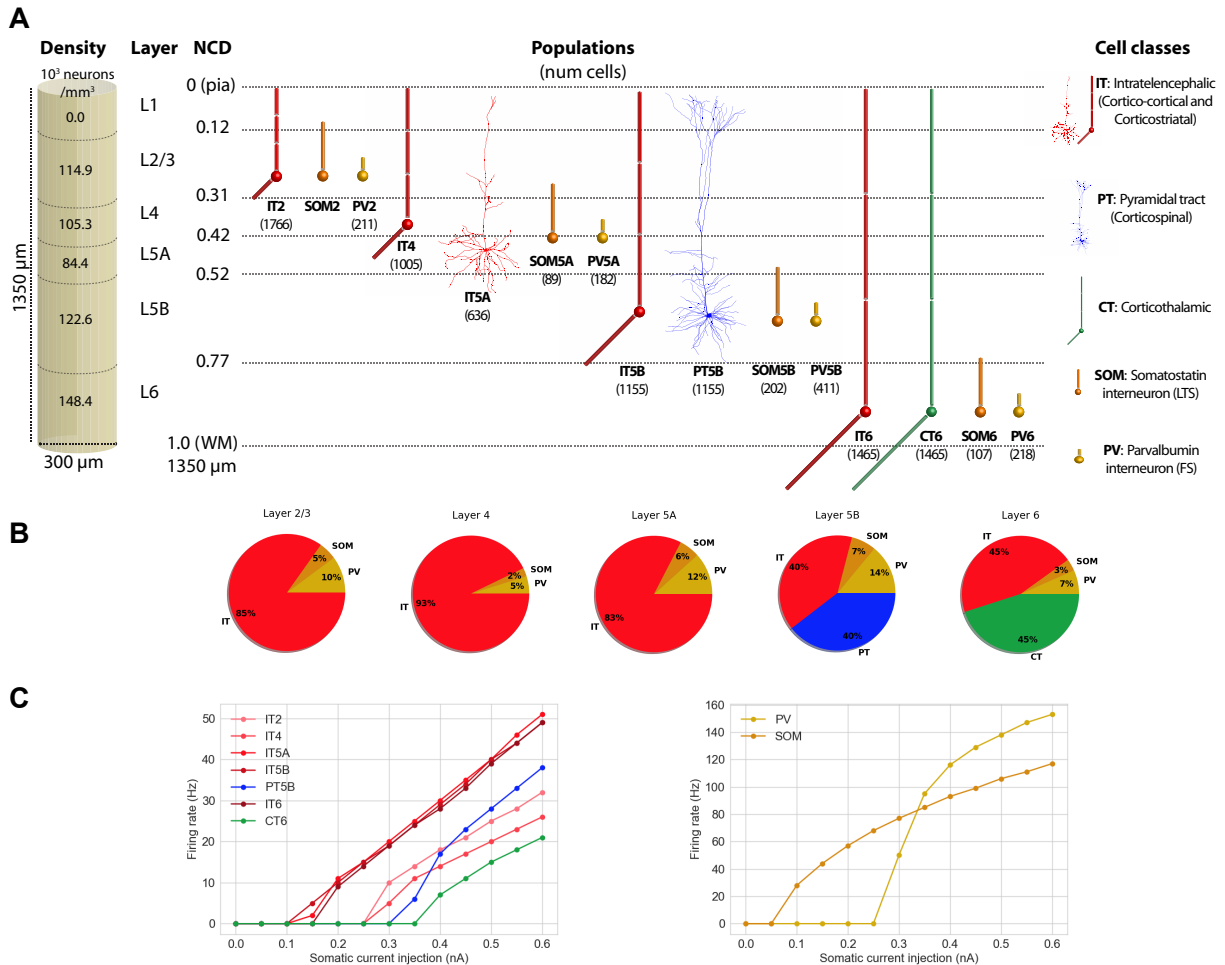


Figure 1: Microcircuit dimensions and neuron densities, composition, classes, morphologies and f-I response. A) Volume, cell density per layer, populations, number of cells, and morphologies; B) Proportion of cell classes per layer; C) f-I curve for each excitatory and inhibitory cell class. All properties were derived from published experimental data. Populations labels include the cell class and layer, e.g. 'IT2' represents the IT cell neurons in layer 2/3.

[68, 2, 70]. Although traditionally M1 has been considered an agranular area lacking layer 4, we recently identified M1 pyramidal neurons with the expected prototypical physiological, morphological and wiring properties of layer 4 neurons [70], and therefore incorporated this layer in the model.

Cell classes present in each layer were determined based on mouse M1 studies [18, 62, 2, 70, 49, 30, 45]. IT cell populations were present in all layers, whereas the PT cell population was confined to layer 5B, and the CT cell population only occupied layer 6. SOM and PV interneuron populations were distributed in each layer, with layer 4 and 5B sharing the same populations. Neuronal densities (neurons per mm³) for each layer Fig. 1A were taken from a histological and imaging study of mouse agranular cortex [65]. The proportion of excitatory to inhibitory neurons per layer was obtained from mouse S1 data [34]. The proportion of IT to PT and IT to CT cells in layers 5B and 6, respectively, were both estimated as 1:1 [18, 62, 71]. The ratio of PV to SOM neurons per layer was estimated as 2:1 based on mouse M1 and S1 studies [27, 67] (Fig. 1B). Since data for M1 layer 4 wasn't available, interneuron populations labeled PV5A and SOM5A occupy both layers 4 and 5A. The number of cells for each population was calculated based on the modeled cylinder dimensions, layer boundaries and neuronal

proportions and densities per layer.

2.3 Local connectivity

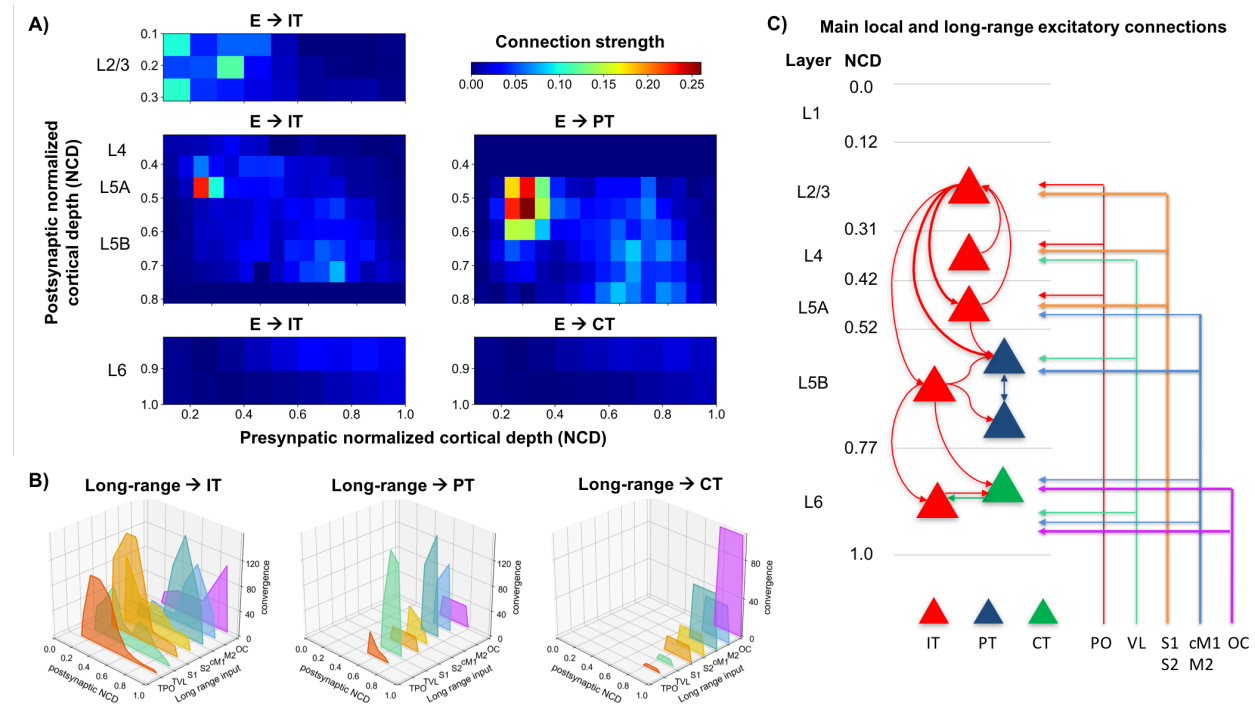


Figure 2: M1 excitatory connectivity: local microcircuitry and long-range inputs. A) Strength of local excitatory connections as a function of pre- and post-synaptic normalized cortical depth (NCD) and post-synaptic cell class; B) Convergence of long-range excitatory inputs from seven thalamic and cortical regions as a function post-synaptic NCD and cell class; C) Schematic of main local and long-range excitatory connections (thin line: medium; thick line: strong).

We calculated local connectivity between M1 neurons Fig. 2A by combining data from multiple studies. Data on excitatory inputs to excitatory neurons (IT, PT and CT) was primarily derived from mapping studies using whole-cell recording, glutamate uncaging-based laser-scanning photostimulation (LSPS) and channelrhodopsin-2-assisted circuit mapping (CRACM) analysis [68, 2, 70, 71]. Connectivity data was postsynaptic cell class-specific and employed normalized cortical depth (NCD) instead of layers as the primary reference system. Unlike layer definitions which are interpreted differently, NCD provides a well-defined, consistent and continuous reference system, depending only on two readily-identifiable landmarks: pia (NCD=0) and white matter (NCD=1). Incorporating NCD-based connectivity into our model allowed us to capture wiring patterns down to a 100 μm spatial resolution, well beyond traditional layer-based cortical models. M1 connectivity varied systematically within layers. For example, the strength of inputs from layer 2/3 to L5B corticospinal cells depends significantly on cell soma depth, with upper neurons receiving much stronger input [2].

Connection strength thus depended on presynaptic NCD and postsynaptic NCD and cell class. For postsynaptic IT neurons with NCD ranging from 0.0 to 0.3125 (layer 2/3) and 0.8125 to 1.0 (layer 6) we determined connection strengths based on data from [68] with cortical depth resolution of 140 μm -resolution. For postsynaptic IT and PT neurons with NCD between 0.3125 and 0.8125 (layers 4, 5A and 5B) we employed connectivity strength data from [2] with cortical depth resolution of 100 μm . For postsynaptic CT neurons in layer 6 we used the same connection strengths as for layer 6 IT cells [68], but reduced to 62% of original values, following published data on the circuitry of M1 CT neurons [71].

Diagonal elements in the connectivity matrices were increased by 20% to compensate for the underestimates resulting from LSPS CRACM analysis. Our data [71] also suggested that connection strength from layer 4 to layer 2/3 IT cells was similar to that measured in S1, so for these projections we employed values from Lefort’s S1 connectivity strength matrix [34]. Experimentally, these connections were found to be four times stronger than in the opposite direction – from layer 2/3 to layer 4 – so we decreased the latter in the model to match this ratio.

Following previous publications [28, 34], we defined connection strength (s_{con}) between two populations, as the product of their probability of connection (p_{con}) and the unitary connection somatic EPSP amplitude in mV (i_{con}), i.e. $s_{con} = p_{con} \times i_{con}$. We employed this equivalence to disentangle the connection s_{con} values provided by the above LSPS studies into p_{con} and i_{con} values that we could use to implement the model. First, we rescaled the LSPS raw current values in pA [2, 68, 70, 71] to match s_{con} data from a paired recording study of mouse M1 L5 excitatory circuits [28]. Next, we calculated the M1 NCD-based i_{con} matrix by interpolating a layerwise unitary connection EPSP amplitude matrix of mouse S1 [34], and thresholding values between 0.3 and 1.0 mV. Finally, we calculated the probability of connection matrix as $p_{con} = s_{con}/i_{con}$.

To implement i_{con} values in the model we calculated the required NEURON connection weight of an excitatory synaptic input to generate a somatic EPSP of 0.5 mV at each neuron segment. This allowed us to calculate a scaling factor for each segment that converted i_{con} values into NEURON weights, such that the somatic EPSP response to a unitary connection input was independent of synaptic location. This is consistent with experimental evidence showing synaptic conductances increased with distance from soma, to normalize somatic EPSP amplitude of inputs within 300 μm of soma [38]. Following this study, scaling factor values above 4.0 – such as those calculated for PT cell apical tufts – were thresholded to avoid overexcitability in the network context where each cell receives hundreds of inputs that interact nonlinearly [60, 4]. For morphologically detailed cells (layer 5A IT and layer 5B PT), the number of synaptic contacts per unitary connection (or simply, synapses per connection) was set to five, an estimated average consistent with the limited mouse M1 data [22] and rat S1 studies [6, 40]. Individual synaptic weights were calculated by dividing the unitary connection weight (i_{con}) by the number of synapses per connection. Although the method does not account for nonlinear summation effects [60], it provides a reasonable approximation and enables employing a more realistic number and spatial distribution of synapses, which may be key for dendritic computations [36]. For the remaining cell models, all with six compartments or less, a single synapse per connection was used.

For excitatory inputs to inhibitory cell types (PV and SOM) we started with the same values as for IT cell types but adapted these based on the specific connectivity patterns reported for mouse M1 interneurons [3, 71] Fig. 2A. Following the layer-based description in these studies, we employed three major subdivisions: layer 2/3 (NCD 0.12 to 0.31), layers 4, 5A and 5B (NCD 0.31 to 0.77) and layer 6 (NCD 0.77 to 1.0). We increased the probability of layer 2/3 excitatory connections to layers 4, 5A and 5B SOM cells by 50% and decreased that to PV cells by 50% [3]. We implemented the opposite pattern for excitatory connections arising from layer 4,5A,5B IT cells such that PV interneurons received stronger intralaminar inputs than SOM cells [3]. The model also accounts for layer 6 CT neurons generating relatively more inhibition than IT neurons [71]. Inhibitory connections from interneurons (PV and SOM) to other cell types were limited to neurons in the same layer [27], with layers 4, 5A and 5B combined into a single layer [45]. Probability of connection decayed exponentially with the distance between the pre- and post-synaptic cell bodies with length constant of 100 μm [15, 14].

Excitatory synapses consisted of colocalized AMPA (rise, decay τ : 0.05, 5.3 ms) and NMDA (rise, decay τ : 15, 150 ms) receptors, both with reversal potential of 0 mV. The ratio of NMDA to AMPA receptors was 1.0 [44], meaning their weights were each set to 50% of the connection weight. NMDA conductance was scaled by $1/(1 + 0.28 \cdot \text{Mg} \cdot \exp(-0.062 \cdot V))$; $\text{Mg} = 1\text{mM}$ [26]. Inhibitory synapses from SOM to excitatory neurons consisted of a slow GABAA receptor (rise, decay τ : 2, 100 ms) and GABAB receptor, in a 90% to 10% proportion; synapses from SOM to inhibitory neurons only included the slow GABAA receptor; and synapses from PV to other neurons consisted of a fast GABAA receptor (rise, decay τ : 0.07, 18.2). The reversal potential was -80 mV for GABAA and -95 mV for GABAB. The GABAB

synapse was modeled using second messenger connectivity to a G protein-coupled inwardly-rectifying potassium channel (GIRK) [11]. The remaining synapses were modeled with a double-exponential mechanism.

Connection delays were estimated as 2 ms plus a variable delay depending on the distance between the pre- and postsynaptic cell bodies assuming a propagation speed of 0.5 m/s.

2.4 Long-range input connectivity

We added long-range input connections from seven regions that are known to project to M1: thalamus posterior nucleus (TPO), ventro-lateral thalamus (TVL), primary somatosensory cortex (S1), secondary somatosensory cortex (S2), contralateral primary motor cortex (cM1), secondary motor cortex (M2) and orbital cortex (OC). Each region consisted of a population of 1000 [9, 6] spike-generators (NEURON VecStims) that generated independent random Poisson spike trains with uniform distributed rates between 0 and 2 Hz [69, 20]; or 0 to 20 Hz [23, 25] when simulating increased input from a region. Previous studies provided a measure of normalized input strength from these regions as a function of postsynaptic cell type and layer or NCD. Broadly, TPO [70, 71, 45], S1 [39] and S2 [63] projected strongly to IT cells in layers 2/3, 4 and 5A; TVL projected strongly to PT cells and moderately to IT cells [70, 71, 45]; cM1 and M2 projected strongly to IT and PT cells in layers 5B and 6 [21]; and OC projected strongly to layer 6 CT and IT cells [21]. We implemented these relations by estimating the maximum number of synaptic inputs from each region and multiplying that value by the normalized input strength for each postsynaptic cell type and NCD range. This resulted in a convergence value – average number of synaptic inputs to each postsynaptic cell – for each projection Fig. 2B. We fixed all connection weights (unitary connection somatic EPSP amplitude) to 0.5 mV, consistent with rat and mouse S1 data [22, 9].

To estimate the maximum number of synaptic inputs per region, we made a number of assumptions based on the limited data available Fig. 2B. First, we estimated the average number of synaptic contacts per cell as 8234 by rescaling rat S1 data [42] based on our own observations for PT cells [62] and contrasting with related studies [56, 10]; we assumed the same value for all cell types so we could use convergence to approximate long-range input strength. We assumed 80 % of synaptic inputs were excitatory vs. 20 % inhibitory [10, 40]; out of the excitatory inputs, 80 % were long-range vs. 20 % local [40, 61]; and out of the inhibitory inputs, 30 % were long-range vs. 70 % local [61]. Finally, we estimated the percentage of long-range synaptic inputs arriving from each region based on mouse brain mesoscale connectivity data [48] and other studies [41, 6, 42, 72, 5]: TVL, S1, cM1 each contributed 15 %, whereas TPO, S2, M2 and OC each accounted for 10 %.

2.5 Dendritic distribution of synaptic inputs

Experimental evidence demonstrates the location of synapses along dendritic trees follows very specific patterns of organization that depend on the brain region, cell type and cortical depth [51, 63]; these are likely to result in important functional effects [32, 33, 60]. We employed subcellular Channelrhodopsin-2-Assisted Circuit Mapping (sCRACM) data to estimate the synaptic density along the dendritic arbor – 1D radial axis – for inputs from TPO, TVL, M2 and OC to layers 2/3, 5A, 5B and 6 IT and CT cell [21] (Fig. 3A), and for layer 2/3 IT, TVL, S1, S2, cM1 and M2 to PT neurons [63] (Fig. 3B). To approximate radial synaptic density we divided the sCRACM map amplitudes by the dendritic length at each grid location, and averaged across rows. Once all network connections had been generated, synaptic locations were automatically calculated for each cell based on its morphology and the pre- and postsynaptic cell type-specific radial synaptic density function (Fig. 3C). Synaptic inputs from PV to excitatory cells were located perisomatically (50 μm around soma); SOM inputs targeted apical dendrites of excitatory neurons [45, 27]; and all inputs to PV and SOM cells targeted apical dendrites. For projections where no data synaptic distribution data was available – IT/CT, S1, S2 and cM1 to IT/CT cells – we assumed a uniform dendritic length distribution.

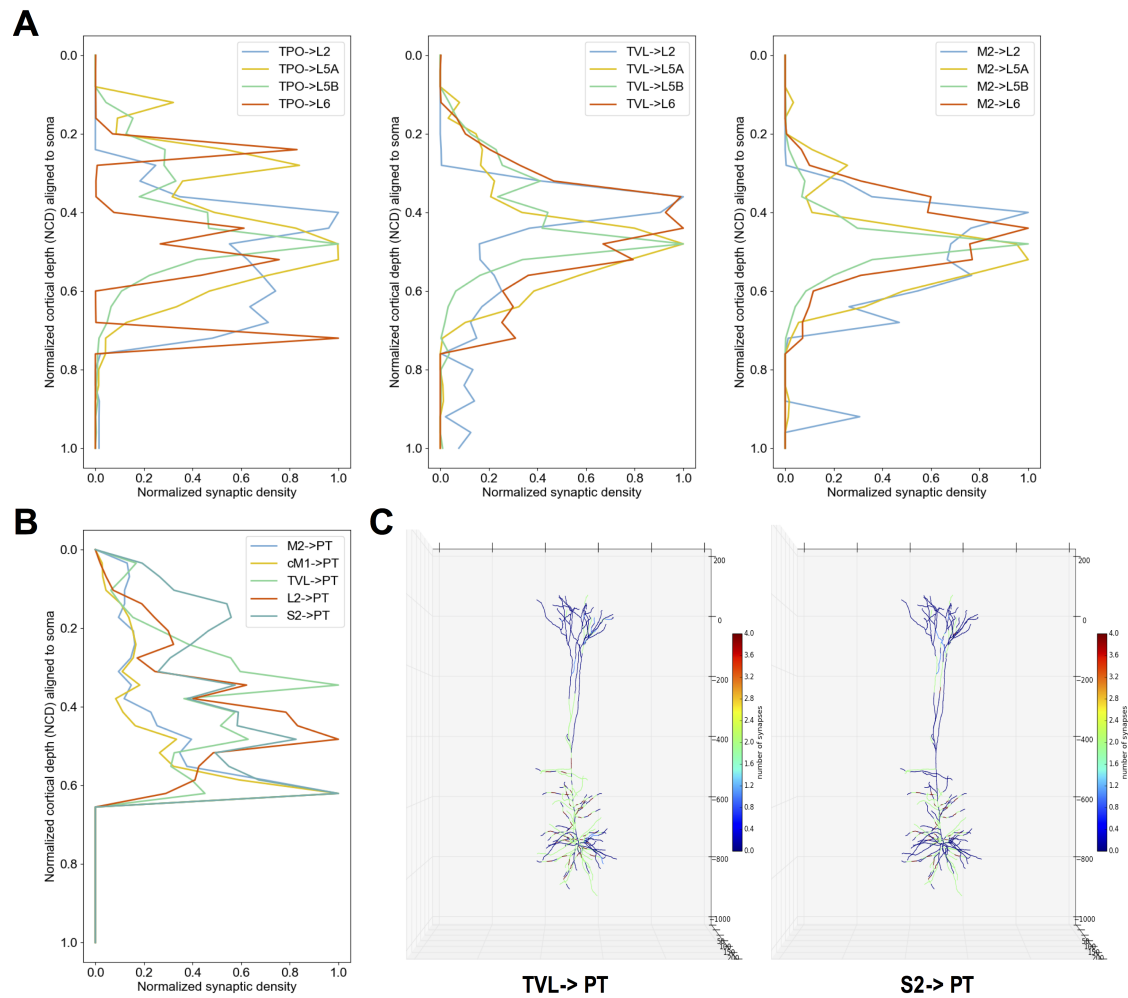


Figure 3: **Dendritic distribution of synaptic inputs.** Synaptic density profile (1D) along the dendritic arbor for inputs from A) TPO, TVL, M2 and OC to layers 2/3, 5A, 5B and 6 IT and CT cells; and B) layer 2/3 IT, TVL, S1, S2, cM1 and M2 to PT neurons. C) Synaptic locations automatically calculated for each cell based on its morphology and the pre- and postsynaptic cell type-specific radial synaptic density function. Here TVL- \rightarrow PT and S2- \rightarrow PT are compared and exhibit partially complementary distributions.

2.6 Model implementation, simulation and analysis

The model was developed using parallel NEURON [37] and NetPyNE [55] (www.neurosimplab.org/netpyne), a Python package to facilitate the development of biological neuronal networks in the NEURON simulator. NetPyNE emphasizes the incorporation of multiscale anatomical and physiological data at varying levels of detail. It converts a set of simple, standardized high-level specifications in a declarative format into a NEURON model. NetPyNE also facilitates organizing and running parallel simulations by taking care of distributing the workload and gathering data across computing nodes. It also provides a powerful set of analysis methods so the user can plot spike raster plots, LFP power spectra, information transfer measures, connectivity matrices, or intrinsic time-varying variables (eg. voltage) of any subset of cells. To facilitate data sharing, the package saves and loads the specifications, network, and simulation results using common file formats (Pickle, Matlab, JSON or HDF5), and can convert to and from NeuroML, a standard data format for exchanging models in computational neuroscience. Simulations were run on XSEDE supercomputers Comet and Stampede using the Neuroscience Gateway (NSG) and our own resource allocation.

3 Results

3.1 Activity patterns in M1 network

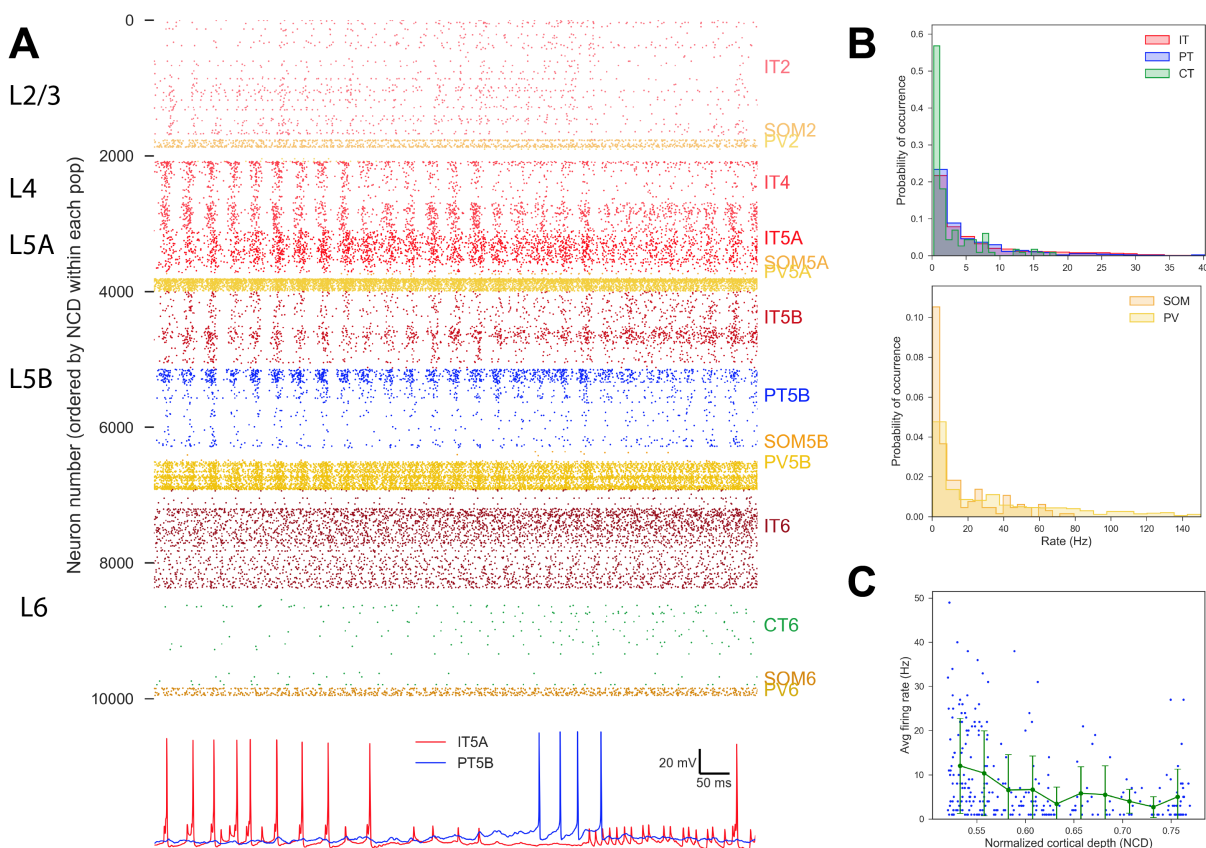


Figure 4: **Cell type-, layer- and sublayer-specific M1 activity with background generated by long-range inputs.** A) *Top*: 1 sec raster plot. Cells are grouped by population and ordered by NCD within each population. Note that no lines are given for the locations of the particular layers since those boundaries are always somewhat indeterminate (a motivation for using NCD). *Bottom*: Example IT5A and PT5B voltage traces. B) Distribution of average firing rates for the different classes of excitatory ((top)) and inhibitory ((bottom)) (across 4 seconds). C) Scatter plot (blue dots) and binned mean and standard deviation (green line) of PT5B firing rates as a function of cell normalized cortical depth (NCD) (across 4 seconds).

We characterized expected *in vivo* spontaneous activity that would be driven by long-range inputs from the 7 characterized input regions firing at a baseline level distributed uniformly for each input stream in range of 0 to 2 Hz (Fig. 4). Overall firing rates ranged up to 20 Hz for excitatory populations, with 40 Hz for inhibitory populations, consistent with the *in vivo* recordings from multiple cortical areas in rat and mouse [23, 35, 50, 13]. Additionally, the distribution of cell average firing rates was highly skewed and long tailed, providing a lognormal distribution (Fig. 4B).

Activity patterns were not only dependent on cell class and cortical-layer location, but also sublaminal location, demonstrating the importance of identifying connectivity and organizing simulations by NCD rather than layer [18, 2]. PT cell activity within layer 5B was particularly high at the top of L5b and decreased with cortical depth (Fig. 4C), consistent with the strong sublaminal targeting of local projections and of long-range connections [2, 68].

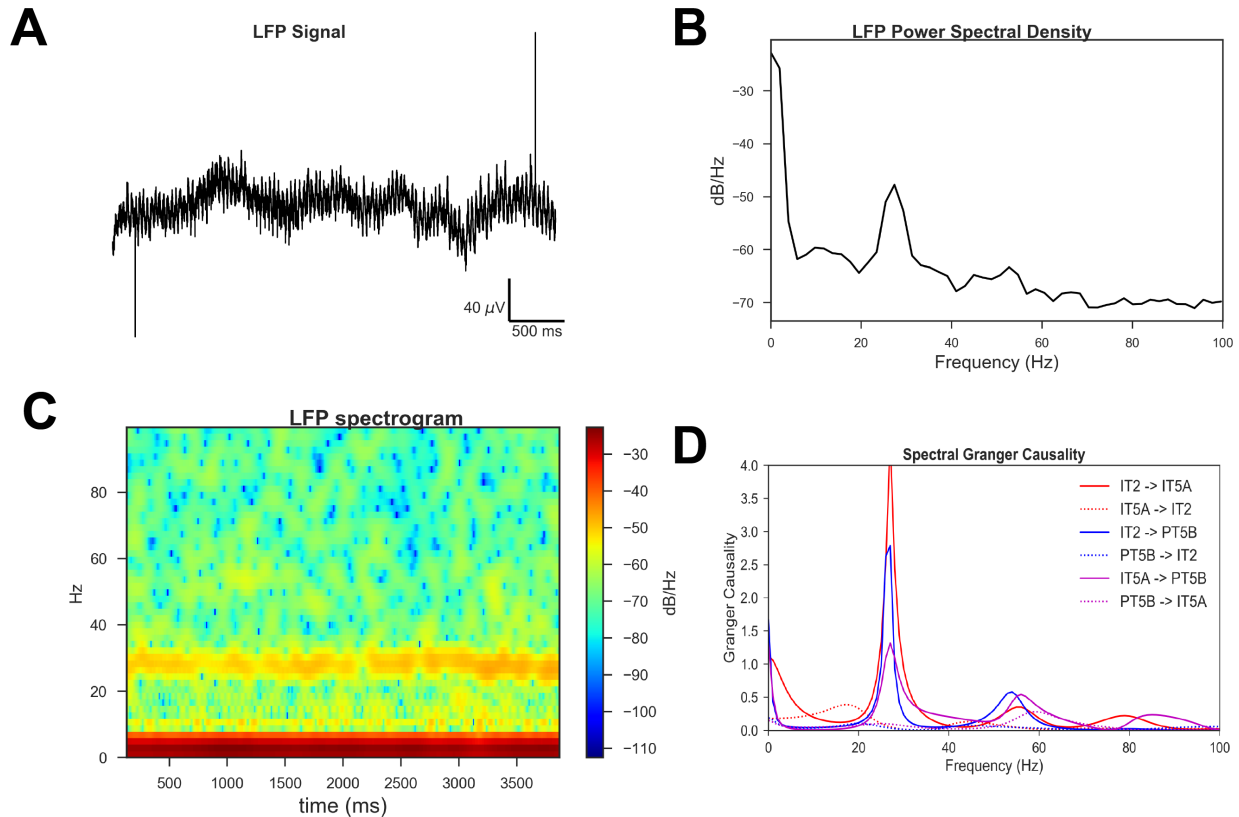


Figure 5: **Local field potential (LFP) and Granger causality during spontaneous activity.** A) LFP signal averaged across 11 recording electrodes at different depths (200 μm to 1300 μm at 1300 μm interval). B) Power spectral density (PSD) with peaks at beta and gamma frequencies, characteristic of cortical activity. Physiological oscillations emerged in the absence of rhythmic external inputs. C) LFP spectrogram with a consistently strong beta frequency peak and weaker gamma frequency peaks across 4 seconds. D) Spectral Granger causality shows strong information flow at beta frequency from IT2 to IT5A and PT5B, and from IT5A to PT5B, but not in the opposite direction.

3.2 Field activity and information flow

Simulated LFP recordings from the M1 model revealed physiological oscillations in the beta and gamma range (Fig. 5). These emerged in the absence of rhythmic external inputs, and are therefore a consequence of neuronal biophysical properties and circuit connectivity. To our knowledge, this is the first data-driven, biophysically-detailed model of M1 microcircuits that exhibits spontaneous physiological oscillations without rhythmic synaptic inputs. Beta-band oscillations peaked at 28 Hz and were robust across the full 4-second simulation; gamma oscillations were weaker and its peak varied across time between 40 and 80 Hz (Fig. 5B,C). Strong LFP beta and gamma oscillations are characteristic of motor cortex activity in both rodents [8, 66] and monkeys [54, 47]. Spectral Granger Causality analysis revealed strong information flow from IT2 cells to IT5A and PT5B, and from IT5A to PT5B, but not from PT5B to upper layer IT cells (Fig. 5D). These results confirm information flow follows known microcircuit functional connectivity depicting M1 as a system with a preprocessing-like upper-layer loop that unidirectionally drives lower-layer output circuits [68]. Information flow frequency peaks coincided with LFP beta and gamma bands, both of which play a predominant role in information coding during preparation and execution of movements [1, 66].

3.3 Sensory-related pathways and H-current modulation

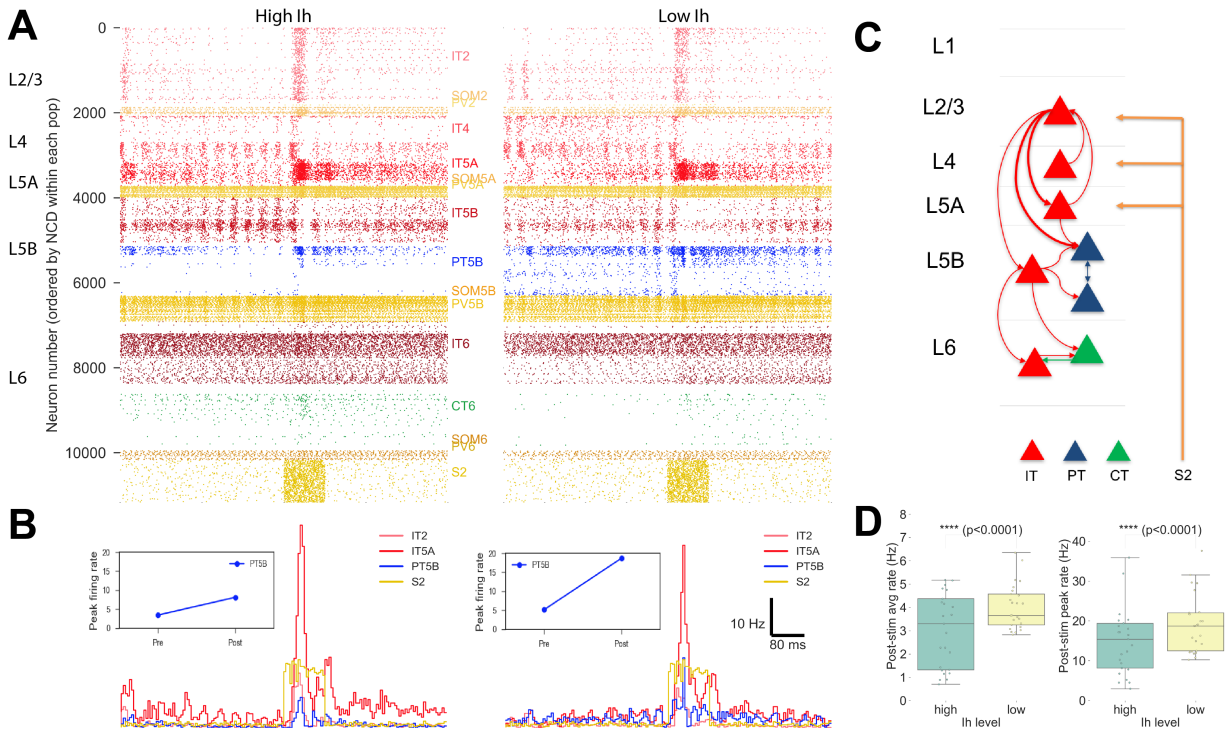


Figure 6: **M1 response to S2 input for high vs. low PT I_h levels.** A) Raster plots of M1 in response to increased S2 activity (15 Hz for 100 ms) after 400 ms, with high (left) vs low (right) PT5B I_h . B) Temporal spike histogram of S2, IT2, IT5A and PT5B populations for high vs low PT I_h level; inset figures shows PT5B peak rate before and after S2 pulse. High I_h results in IT-predominant mode, whereas low I_h results in a mixed mode with both IT and PT activity. C) Schematic of main pathways activated due to S2 increased activity. D) Boxplot analysis showing statistically significant higher average and peak PT5B firing rate in response to S2 input for low vs. high PT5B I_h level. Analysis performed across 25 simulations with 5 different connectivity randomization seeds \times 5 different spiking input randomization seeds.

Modulation of H-current level in conjunction with sensory-related long-range inputs lead to different modes of operation in M1. Increased rates (average 15 Hz for 100 ms) in PO, S1 or S2 together with an upregulated H-current favored an IT-predominant mode (with low PT activity) – Fig. 6 (high I_h) shows results for the S2 input case. The same long-range input levels with H-current downregulated lead to a mixed mode where upper layer IT cells in turn activated PT cells (Fig. 6, low I_h case). Analysis across 25 simulations with different wiring and input randomization seeds demonstrated a statistically significant increase in PT5B average and peak firing rates for low vs. high I_h . Downregulation of H-current facilitated synaptic integration of inputs and increased PT output activity. This constitutes one of the pathways that can generate corticospinal output: sensory-related inputs projecting to superficial IT neurons in turn exciting PT cells.

3.4 Motor-related pathways and H-current modulation

Motor-related inputs bypassing upper M1 layers and directly projecting to PT cells constitute a second pathway that can result in corticospinal output. Increased activation (average 15 Hz for 100 ms) of VL, cM1 and M2 inputs with downregulated H-current promoted a PT-predominant mode with lower IT activity – Fig. 7 (low I_h) shows results for the M2 input case. As with sensory-related inputs, upregulation of H-current in corticospinal cells also decreased their activity (Fig. 7 high I_h). Analysis across 25

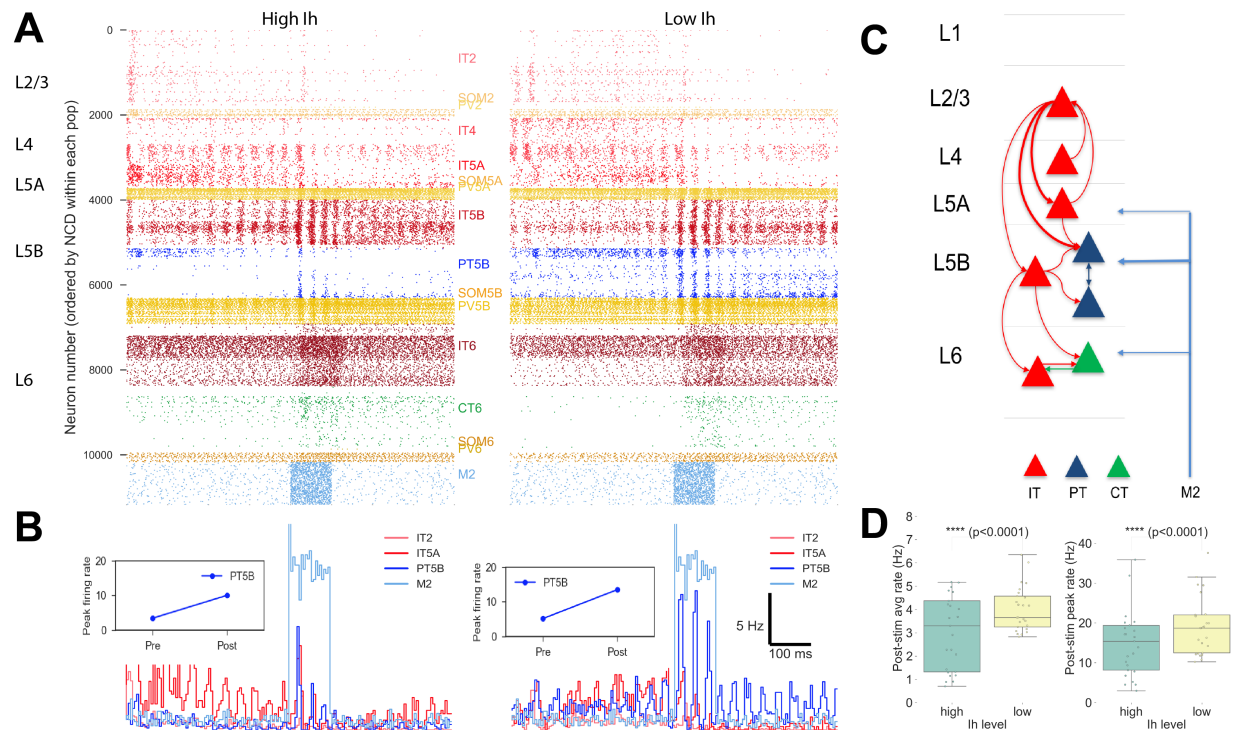


Figure 7: M1 response to M2 input for high vs. low PT I_h levels. A) Raster plots of M1 in response to increased M2 activity (15 Hz for 100 ms) after 400 ms, with high (left) vs low (right) PT5B I_h . B) Temporal spike histogram of M2, IT2, IT5A and PT5B populations for high vs low PT I_h level; inset figures show PT5B peak rate before and after M2 pulse. Low I_h level results in PT-predominant mode. C) Schematic of main pathways activated due to M2 increased activity. D) Boxplot analysis showing statistically significant higher average and peak PT5B firing rate in response to M2 input for low vs. high PT5B I_h level. Analysis performed across 25 simulations with 5 different connectivity randomization seeds \times 5 different spiking input randomization seeds.

simulations with different wiring and input randomization seeds demonstrated a statistically significant increase in PT5B average and peak firing rates for low vs. high I_h . This effect was stronger than for sensory-related inputs.

3.5 Interaction between sensory- and motor-related pathways and H-current modulation

M1 response to increased activation from S2 and M2 inputs depended strongly on the order of presentation, interval between inputs and PT I_h level (Fig. 8). For IT5A cells, lower I_h increased activity only when the S2 input occurred before M2. IT5A activity exhibited significantly stronger average and peak rates when S2 was presented before M2. In that case, average IT5A rates increased with interval indicating summation of inputs; whereas with M2 inputs first, there was no clear pattern in relation to interval. Peak IT5A rates plateaued after 20 ms interval when S2 was presented first, indicating peak was determined by the S2 input. However, when M2 was presented first, IT5A rates showed the inverse pattern, decreasing proportional to interval, suggesting dominance of the M2 input.

Lower I_h consistently resulted in higher activity in PT5B neurons, independently of order and interval (Fig. 8). PT5B average rate increased with interval if S2 came before M2, but decreased with interval if M2 input was first. This suggests initial S2 input results in PT5B having a longer integration window which enables summation of the M2 inputs. Peak PT5B rates were constant when S2 input arrived first –

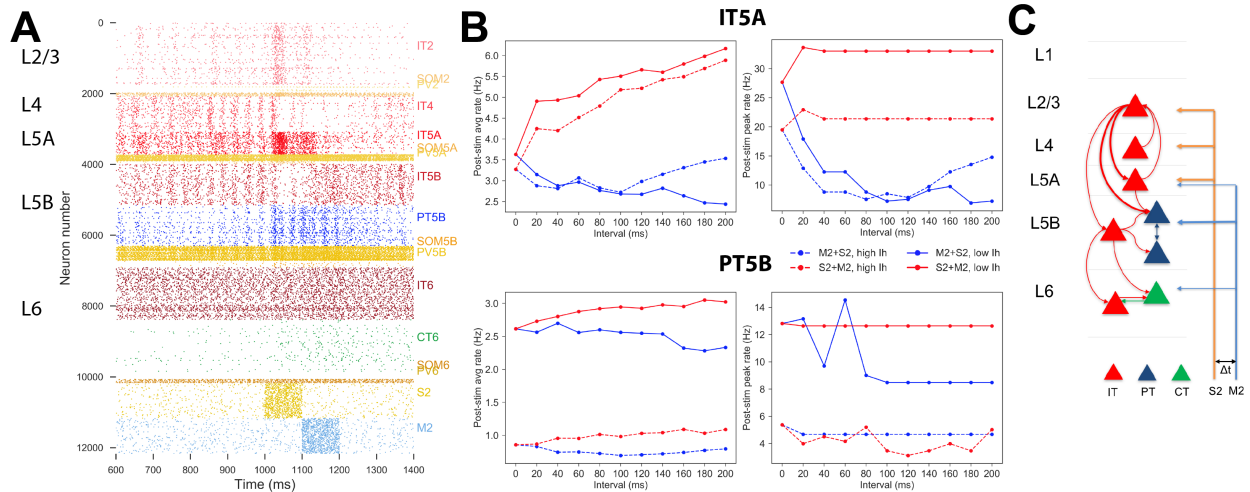


Figure 8: M1 response to S2 and M2 inputs as a function of order and interval of inputs and PT I_h level. A) Raster plot of M1 in response to increased S2 and M2 activity (15 Hz for 100 ms) with S2 starting at 400 ms and M2 100 ms (interval) later; PT5B was low. B) Average (left) and peak (right) post-stimulus IT5A (top) and PT5B (bottom) firing rate for different intervals (x-axis), order of presentation (blue: M2-S2; red: S2-M2), and high (dotted) vs low (solid) I_h levels. C) Schematic of main pathways activated due to S2 and M2 increased activity. Varying interval between presentation of inputs illustrated with δt symbol.

suggesting S2 dictated its peak rate – but presented a strong peak at 60 ms interval when M2 arrived first. This might indicate resonance at the beta frequency range, consistent with our previous observation (Fig. 4).

3.6 Information flow in response to recorded time-varying spiking activity

Time-varying spiking activity recorded from mouse somatosensory cortex – 4 second duration, average rate of 2.77 Hz – was used as S2 input (Fig. 9A). With high I_h , information flow, quantified using Spectral Granger causality, was strongest from S2 to IT5A and was concentrated in the beta frequency range. With low I_h , information flow shifted to the gamma frequency range and was strongest from S2 to PT5B (Fig. 9B). This provides further support for the role of I_h in modulating the flow of information to corticospinal output and switching between the IT-predominant mode and a mixed mode with both IT and PT activity.

A different set of recordings – also 4 second duration, average rate of 3.84 Hz – was simultaneously used as input to M2, to evaluate the interactions between S2 and M2 inputs. With high I_h , information flow was strongest among upper layers (IT2 to IT5A), but was very low from S2 and M2 to any of the local populations. This suggests simultaneous activation resulted in destructive interference of the signal. Lowering I_h resulted in increased information flow peaks at beta frequency from IT2, S2 and M2 to PT5B, again suggesting I_h has a potential mechanism to enable information to reach corticospinal neurons (Fig. 9C).

Recordings of neuron spiking activity in mouse somatosensory cortex were downloaded from CRCNS.org [24]. The recordings were performed in vitro with a large and dense multielectrode array. The data represents spontaneous activity given that the culture was not stimulated. Spike trains were filtered to include only those with an average firing rate between 0.1 and 50 Hz.

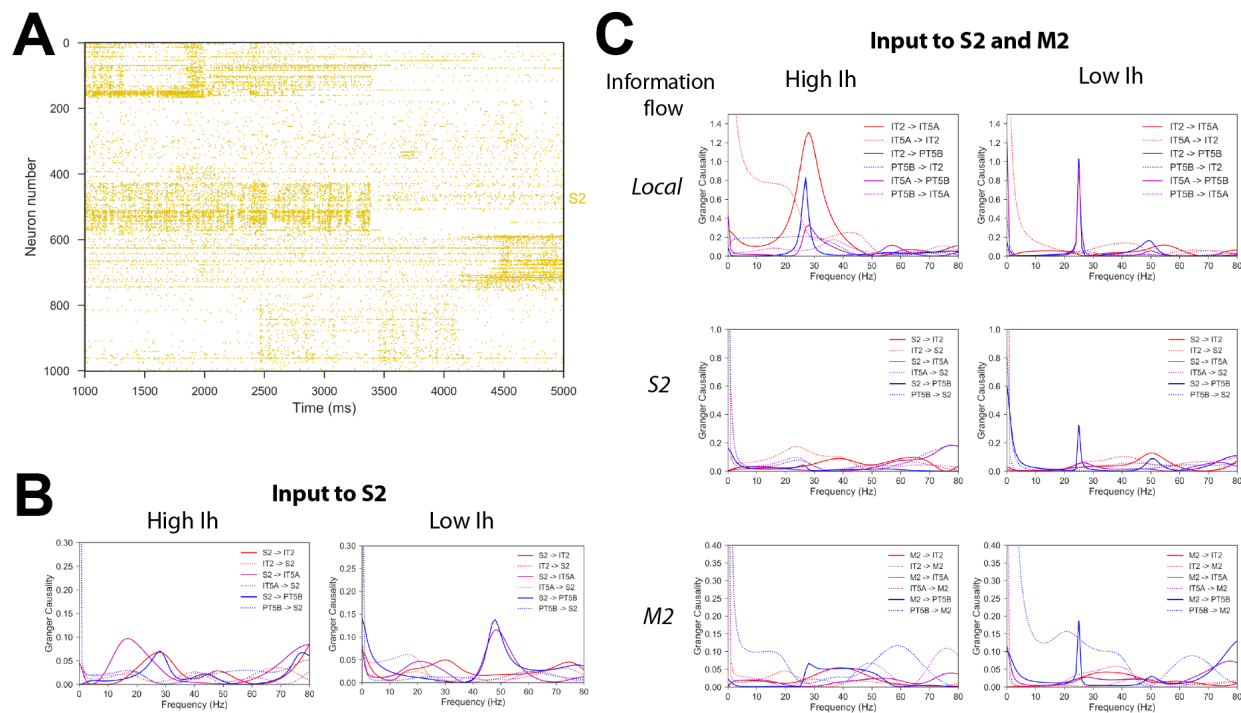


Figure 9: Information flow in M1 in response to time-varying spiking activity recorded from mouse somatosensory cortex. A) Raster plot of time-varying spiking activity recorded from mouse somatosensory cortex. B) Spectral Granger causality when using the recorded spiking data (A) as input to S2; shows increase of information flow from S2 to PT5B in the gamma frequency range for low vs. high I_h . C) Spectral Granger causality between populations when using the recorded spiking data (A) as input to M2 and a different recorded pattern as input to S2; shows increase in information flow from upper layer ITs (IT2 and IT5A) to PT5B and from long-range inputs (S2 and M2) to PT5B in the beta frequency range for low vs. high I_h .

4 Discussion

In this study we developed the most detailed computational model of mouse M1 microcircuits and corticospinal neurons up to date, based on an accumulated set of experimental studies. Overall, the model incorporates quantitative experimental data from 15 publications, thus integrating previously isolated knowledge into a unified framework. Unlike the real brain, this in silico system serves as a testbed that can be probed extensively and precisely, and can provide accurate measurements of neural dynamics at multiple scales. We employed the model to evaluate how long-range inputs from surrounding regions and molecular/pharmacological-level effects (e.g. regulation of HCN channel) modulate M1 dynamics.

The M1 simulation reproduced several experimental observations. The reported lognormal distribution of firing rates in our model has been found extensively in cortical networks [53, 31]. The simulation tied a key structural property – different upper vs lower layer 5B wiring – to differentiated circuit-level neural dynamics and function – higher activity in upper layer 5B. The LFP beta and gamma oscillations have been measured in rodent and primate motor cortices and may be fundamental to the relation of brain structure and function [7].

We simulated the inputs from the main cortical and thalamic regions that project to M1, based on recent experimental data from optogenetic mapping studies. Consistent with experimental data [21, 63], this study evidenced two different pathways that can generate corticospinal output: motor-related inputs from VL, cM1 or M2 regions bypassing upper M1 layers and directly projecting to corticospinal cells, and

sensory-related inputs from PO, S1 and S2 regions projecting to superficial IT neurons in turn exciting layer 5B corticospinal cells. Activation of OC region lead to increased layer 6 IT and CT activity and physiological oscillations in the beta and gamma range. Downregulation of corticospinal H-current lead to increased firing rate and information flow, as observed experimentally. This has been hypothesized as a potential mechanism to translate action planning into action execution [57]. Our model also provides insights into the interaction between sensory- and motor-related inputs, suggesting that the order and interval between inputs determines its effect on corticostriatal and corticospinal responses.

Our study provides insights to help decipher the neural code underlying the brain circuits responsible for producing movement, and help understand motor disorders, including spinal cord injury. The computational model provides a framework to integrate experimental data and can be progressively extended as new data becomes available. This provides a useful tool for researchers in the field, who can use the framework to evaluate hypothesis and guide the design of new experiments. A recent study on closed-loop optogenetics suggests employing models of cortical microcircuits to guide patterned stimulation that restores healthy neural activity [17].

5 Acknowledgements

This work was funded by the following grants: NIH U01EB017695, NYS SCIRB DOH01-C32250GG-3450000 and NIH R01EB022903.

References

- [1] Matt Ainsworth, Shane Lee, Mark O. Cunningham, Roger D. Traub, Nancy J. Kopell, and Miles A. Whittington. Rates and rhythms: A synergistic view of frequency and temporal coding in neuronal networks. *Neuron*, 75(4):572 – 583, 2012.
- [2] Charles T. Anderson, Patrick L. Sheets, Taro Kiritani, and Gordon M. G. Shepherd. Sublayer-specific microcircuits of corticospinal and corticostriatal neurons in motor cortex. *Nature neuroscience*, 13(6):739–44, June 2010.
- [3] Alfonso J Apicella, Ian R Wickersham, H Sebastian Seung, and Gordon MG Shepherd. Laminarly orthogonal excitation of fast-spiking and low-threshold-spiking interneurons in mouse motor cortex. *The Journal of Neuroscience*, 32(20):7021–7033, 2012.
- [4] Bardia F Behabadi, Alon Polsky, Monika Jadi, Jackie Schiller, and Bartlett W Mel. Location-dependent excitatory synaptic interactions in pyramidal neuron dendrites. *PLoS Comput Biol*, 8(7):e1002599, 2012.
- [5] Rita Bopp, Simone Holler-Rickauer, Kevan AC Martin, and Gregor FP Schuhknecht. An ultrastructural study of the thalamic input to layer 4 of primary motor and primary somatosensory cortex in the mouse. *Journal of Neuroscience*, 37(9):2435–2448, 2017.
- [6] Randy M Bruno and Bert Sakmann. Cortex is driven by weak but synchronously active thalamocortical synapses. *Science*, 312(5780):1622–1627, 2006.
- [7] György Buzsáki and Kenji Mizuseki. The log-dynamic brain: how skewed distributions affect network operations. *Nature Reviews Neuroscience*, 15(4):264, 2014.
- [8] Manuel A Castro-Alamancos. The motor cortex: a network tuned to 7-14 hz. *Frontiers in Neural Circuits*, 7(21), 2013.
- [9] Christine M Constantinople and Randy M Bruno. Deep cortical layers are activated directly by thalamus. *Science*, 340(6140):1591–1594, 2013.

- [10] Javier DeFelipe, Lidia Alonso-Nanclares, and Jon I Arellano. Microstructure of the neocortex: comparative aspects. *Journal of neurocytology*, 31(3-5):299–316, 2002.
- [11] A Destexhe, T Bal, DA McCormick, and TJ Sejnowski. Ionic mechanisms underlying synchronized oscillations and propagating waves in a model of ferret thalamic slices. *J Neurophysiol*, 76:2049–2070, 1996.
- [12] RJ Douglas, KAC Martin, and D Whitteridge. A canonical microcircuit for neocortex. *Neural Computation*, 1:480–488, 1989.
- [13] Luc Estebanez, Diana Hoffmann, Birgit C. Voigt, and James F. A. Poulet. Parvalbumin-expressing gabaergic neurons in primary motor cortex signal reaching. *Cell Reports*, 20(2):308–318, 2018/01/19.
- [14] Elodie Fino and Rafael Yuste. Dense inhibitory connectivity in neocortex. *Neuron*, 69(6):1188–1203, 2011.
- [15] Eyal Gal, Michael London, Amir Globerson, Srikanth Ramaswamy, Michael W Reimann, Eilif Muller, Henry Markram, and Idan Segev. Rich cell-type-specific network topology in neocortical microcircuitry. *Nat Neurosci*, 20(7):1004–1013, 07 2017.
- [16] Meena S George, LF Abbott, and Steven A Siegelbaum. Hcn hyperpolarization-activated cation channels inhibit epsps by interactions with m-type k+ channels. *Nature neuroscience*, 12(5):577–584, 2009.
- [17] Logan Grosenick, James H. Marshel, and Karl Deisseroth. Closed-loop and activity-guided optogenetic control. *Neuron*, 86(1):106–139, 2016/07/06 2016.
- [18] Kenneth D Harris and Gordon MG Shepherd. The neocortical circuit: themes and variations. *Nature Neuroscience*, 18(2):170–181, 2015.
- [19] Etay Hay, Sean Hill, Felix Schürmann, Henry Markram, and Idan Segev. Models of neocortical layer 5b pyramidal cells capturing a wide range of dendritic and perisomatic active properties. *PLoS Comput Biol*, 7(7):e1002107, 07 2011.
- [20] Akio Hirata and Manuel A Castro-Alamancos. Relief of synaptic depression produces long-term enhancement in thalamocortical networks. *Journal of neurophysiology*, 95(4):2479–2491, 2006.
- [21] Bryan M Hooks, Tianyi Mao, Diego A Gutnisky, Naoki Yamawaki, Karel Svoboda, and Gordon M G Shepherd. Organization of cortical and thalamic input to pyramidal neurons in mouse motor cortex. *J Neurosci*, 33(2):748–760, Jan 2013.
- [22] Hang Hu and Ariel Agmon. Differential excitation of distally versus proximally targeting cortical interneurons by unitary thalamocortical bursts. *Journal of Neuroscience*, 36(26):6906–6916, 2016.
- [23] Yoshikazu Isomura, Rie Harukuni, Takashi Takekawa, Hidenori Aizawa, and Tomoki Fukai. Microcircuitry coordination of cortical motor information in self-initiation of voluntary movements. *Nature neuroscience*, 12(12):1586–1593, 2009.
- [24] Shinya Ito, Fang-Chin Yeh, Nicholas M. Timme, Pawel Hottowy, Alan M. Litke, and John M. Beggs. Spontaneous spiking activity of hundreds of neurons in mouse somatosensory cortex slice cultures recorded using a dense 512 electrode array. *CRCNS.org*, 2016.
- [25] Vincent Jacob, Leopoldo Petreanu, Nick Wright, Karel Svoboda, and Kevin Fox. Regular spiking and intrinsic bursting pyramidal cells show orthogonal forms of experience-dependent plasticity in layer v of barrel cortex. *Neuron*, 73(2):391–404, 2012.
- [26] CE Jahr and CF Stevens. Voltage dependence of NMDA-activated macroscopic conductances predicted by single-channel kinetics. *J Neurosci*, 10(9):3178–3182, 1990b.

- [27] Dennis Katzel, Boris V Zemelman, Christina Buetfering, Markus Wolfel, and Gero Miesenbock. The columnar and laminar organization of inhibitory connections to neocortical excitatory cells. *Nat Neurosci*, 14(1):100–107, Jan 2011.
- [28] Taro Kiritani, Ian R. Wickersham, H. Sebastian Seung, and Gordon M. G. Shepherd. Hierarchical connectivity and connection-specific dynamics in the corticospinal–corticostriatal microcircuit in mouse motor cortex. *The Journal of Neuroscience*, 32(14):4992–5001, 2012.
- [29] MHP Kole, S Hallermann, and GJ Stuart. Single Ih channels in pyramidal neuron dendrites: properties, distribution, and impact on action potential output. *Journal of Neuroscience*, 26(6):1677–1687, 2006.
- [30] XANTHIPPI KONSTANTOUDAKI, Athanasia Papoutsi, Kleanthi Chalkiadaki, Panayiota Poirazi, and Kyriaki Sidiropoulou. Modulatory effects of inhibition on persistent activity in a cortical microcircuit model. *Frontiers in Neural Circuits*, 8:7, 2014.
- [31] Alexei A Koulakov, Tomáš Hromádka, and Anthony M Zador. Correlated connectivity and the distribution of firing rates in the neocortex. *Journal of Neuroscience*, 29(12):3685–3694, 2009.
- [32] Yoshiyuki Kubota, Satoru Kondo, Masaki Nomura, Sayuri Hatada, Noboru Yamaguchi, Alsayed A Mohamed, Fuyuki Karube, Joachim Lübke, and Yasuo Kawaguchi. Functional effects of distinct innervation styles of pyramidal cells by fast spiking cortical interneurons. *eLife*, 4:e07919, jul 2015.
- [33] Jonathan Laudanski, Benjamin Torben-Nielsen, Idan Segev, and Shihab Shamma. Spatially distributed dendritic resonance selectively filters synaptic input. *PLoS Comput Biol*, 10(8):1–10, 08 2014.
- [34] Sandrine Lefort, Christian Tómm, J. C. Floyd Sarria, and Carl C. H. Petersen. The excitatory neuronal network of the c2 barrel column in mouse primary somatosensory cortex. *Neuron*, 61(2):301–316, 2015/10/05 2009.
- [35] Nuo Li, Kayvon Daie, Karel Svoboda, and Shaul Druckmann. Robust neuronal dynamics in premotor cortex during motor planning. *Nature*, 532(7600):459–464, 04 2016.
- [36] Michael London and Michael Häusser. Dendritic computation. *Annu. Rev. Neurosci.*, 28:503–532, 2005.
- [37] William W. Lytton, Alexandra Seidenstein, Salvador Dura-Bernal, Felix Schurmann, RobertAMcDougal, and Michael L Hines. Simulation neurotechnologies for advancing brain research: Parallelizing large networks in neuron. *Neural Computation*, 28:2063–2090, 2016.
- [38] Jeffrey C Magee and Erik P Cook. Somatic epsp amplitude is independent of synapse location in hippocampal pyramidal neurons. *Nature neuroscience*, 3(9):895–903, 2000.
- [39] Tianyi Mao, Deniz Kusefoglu, Bryan M. Hooks, Daniel Huber, Leopoldo Petreanu, and Karel Svoboda. Long-range neuronal circuits underlying the interaction between sensory and motor cortex. *Neuron*, 72(1):111–123, 2016/12/07 2011.
- [40] Henry Markram, Eilif Muller, Srikanth Ramaswamy, Michael W. Reimann, Marwan Abdellah, Carlos Aguado Sanchez, Anastasia Ailamaki, Lidia Alonso-Nanclares, Nicolas Antille, Selim Arsever, Guy Antoine Atenekeng Kahou, Thomas K. Berger, Ahmet Bilgili, Nenad Buncic, Athanassia Chalimourda, Giuseppe Chindemi, Jean-Denis Courcol, Fabien Delalandre, Vincent Delattre, Shaul Druckmann, Raphael Dumusc, James Dynes, Stefan Eilemann, Eyal Gal, Michael Emiel Gevaert, Jean-Pierre Ghobril, Albert Gidon, Joe W. Graham, Anirudh Gupta, Valentin Haenel, Etay Hay, Thomas Heinis, Juan B. Hernando, Michael Hines, Lida Kanari, Daniel Keller, John Kenyon, Georges Khazen, Yihwa Kim, James G. King, Zoltan Kisvarday, Pramod Kumbhar, Sébastien Lasserre, Jean-Vincent Le Bé, Bruno R. C. Magalhães, Angel Merchán-Pérez, Julie Meystre, Benjamin Roy Morrice, Jeffrey Muller, Alberto Muñoz-Céspedes, Shruti Muralidhar, Keerthan Muthurasa, Daniel Nachbaur, Taylor H. Newton, Max Nolte, Aleksandr Ovcharenko, Juan Palacios, Luis Pastor, Rodrigo

- Perin, Rajnish Ranjan, Imad Riachi, José-Rodrigo Rodríguez, Juan Luis Riquelme, Christian Rössert, Konstantinos Sfyraakis, Ying Shi, Julian C. Shillcock, Gilad Silberberg, Ricardo Silva, Farhan Tauheed, Martin Telefont, Maria Toledo-Rodriguez, Thomas Tränkler, Werner Van Geit, Jafet Villafranca Díaz, Richard Walker, Yun Wang, Stefano M. Zaninetta, Javier DeFelipe, Sean L. Hill, Idan Segev, and Felix Schürmann. Reconstruction and simulation of neocortical microcircuitry. *Cell*, 163(2):456–492, 2015/10/09 2015.
- [41] Hanno S Meyer, Verena C Wimmer, Mike Hemberger, Randy M Bruno, Christiaan PJ de Kock, Andreas Frick, Bert Sakmann, and Moritz Helmstaedter. Cell type-specific thalamic innervation in a column of rat vibrissal cortex. *Cerebral Cortex*, 20(10):2287–2303, 2010.
- [42] Hanno S Meyer, Verena C Wimmer, Marcel Oberlaender, Christiaan PJ De Kock, Bert Sakmann, and Moritz Helmstaedter. Number and laminar distribution of neurons in a thalamocortical projection column of rat vibrissal cortex. *Cerebral cortex*, 20(10):2277–2286, 2010.
- [43] Michele Migliore and Rosanna Migliore. Know your current ih: Interaction with a shunting current explains the puzzling effects of its pharmacological or pathological modulations. *PLOS ONE*, 7(5):1–8, 05 2012.
- [44] Chaelon I. O. Myme, Ken Sugino, Gina G. Turrigiano, and Sacha B. Nelson. The nmda-to-ampa ratio at synapses onto layer 2/3 pyramidal neurons is conserved across prefrontal and visual cortices. *Journal of Neurophysiology*, 90(2):771–779, 2003.
- [45] Alexander Naka and Hillel Adesnik. Inhibitory circuits in cortical layer 5. *Frontiers in Neural Circuits*, 10(35), 2016.
- [46] SA Neymotin, BA Suter, S Dura-Bernal, GM Shepherd, M Migliore, and WW Lytton. Optimizing computer models of corticospinal neurons to replicate in vitro dynamics. *J Neurophysiol*, 117:148–162, 2017.
- [47] Yukio Nishimura, Steve I Perlmutter, and Eberhard E Fetz. Restoration of upper limb movement via artificial corticospinal and musculoskeletal connections in a monkey with spinal cord injury. *Frontiers in Neural Circuits*, 7(57), 2013.
- [48] Seung Wook Oh, Julie A Harris, Lydia Ng, Brent Winslow, Nicholas Cain, Stefan Mihalas, Quanxin Wang, Chris Lau, Leonard Kuan, Alex M Henry, et al. A mesoscale connectome of the mouse brain. *Nature*, 508(7495):207–214, 2014.
- [49] Manfred J Oswald, Malinda LS Tantirigama, Ivo Sonntag, Stephanie M Hughes, and Ruth M Empson. Diversity of layer 5 projection neurons in the mouse motor cortex. *Frontiers in Cellular Neuroscience*, 7(174), 2013.
- [50] Andrew E Papale and Bryan M Hooks. Circuit changes in motor cortex during motor skill learning. *Neuroscience*, 2017.
- [51] Leopoldo Petreanu, Tianyi Mao, Scott M Sternson, and Karel Svoboda. The subcellular organization of neocortical excitatory connections. *Nature*, 457(7233):1142–1145, 2009.
- [52] Anton Reiner, Natalie Hart, Wanlong Lei, and Yunping Deng. Corticostriatal projection neurons – dichotomous types and dichotomous functions. *Frontiers in Neuroanatomy*, 4:142, 2010.
- [53] Alex Roxin, Nicolas Brunel, David Hansel, Gianluigi Mongillo, and Carl van Vreeswijk. On the distribution of firing rates in networks of cortical neurons. *The Journal of Neuroscience*, 31(45):16217–16226, 2011.
- [54] Doug Rubino, Kay A Robbins, and Nicholas G Hatsopoulos. Propagating waves mediate information transfer in the motor cortex. *Nat Neurosci*, 9(12):1549–1557, Dec 2006.

- [55] Dura-Bernal Salvador, Suter BA, Neymotin SA, Kerr CC, Quintana A, Gleeson P, Shepherd GMG, and Lytton WW. Netpyne: a python package for neuron to facilitate development and parallel simulation of biological neuronal networks. In *Computational Neuroscience (CNS)*, 2016.
- [56] Almut Schüz and Günther Palm. Density of neurons and synapses in the cerebral cortex of the mouse. *Journal of Comparative Neurology*, 286(4):442–455, 1989.
- [57] Patrick L Sheets, Benjamin A Suter, Taro Kiritani, C Savio Chan, D James Surmeier, and Gordon MG Shepherd. Corticospinal-specific hcn expression in mouse motor cortex: Ih-dependent synaptic integration as a candidate microcircuit mechanism involved in motor control. *Journal of neurophysiology*, 106(5):2216–2231, 2011.
- [58] Gordon M. Shepherd. Corticostriatal connectivity and its role in disease. *Nature Reviews Neuroscience*, 2013.
- [59] Stewart Shipp. The importance of being agranular: a comparative account of visual and motor cortex. *Philosophical Transactions of the Royal Society B: Biological Sciences*, 360(1456):797–814, 2005.
- [60] Nelson Spruston. Pyramidal neurons: dendritic structure and synaptic integration. *Nature Reviews Neuroscience*, 9(3):206–221, 2008.
- [61] Armen Stepanyants, Luis M Martinez, Alex S Ferecskó, and Zoltán F Kisvárdy. The fractions of short-and long-range connections in the visual cortex. *Proceedings of the National Academy of Sciences*, 106(9):3555–3560, 2009.
- [62] Benjamin A Suter, Michele Migliore, and Gordon MG Shepherd. Intrinsic electrophysiology of mouse corticospinal neurons: a class-specific triad of spike-related properties. *Cerebral Cortex*, 23(8):1965–1977, 2013.
- [63] Benjamin A Suter and Gordon MG Shepherd. Reciprocal interareal connections to corticospinal neurons in mouse m1 and s2. *The Journal of Neuroscience*, 35(7):2959–2974, 2015.
- [64] Shreejoy J. Tripathy, Shawn D. Burton, Matthew Geramita, Richard C. Gerkin, and Nathaniel N. Urban. Brain-wide analysis of electrophysiological diversity yields novel categorization of mammalian neuron types. *Journal of Neurophysiology*, 113(10):3474–3489, 2015.
- [65] Philbert S Tsai, John P Kauffhold, Pablo Blinder, Beth Friedman, Patrick J Drew, Harvey J Karten, Patrick D Lyden, and David Kleinfeld. Correlations of neuronal and microvascular densities in murine cortex revealed by direct counting and colocalization of nuclei and vessels. *The Journal of Neuroscience*, 29(46):14553–14570, 2009.
- [66] Yasuhiro Tsubo, Yoshikazu Isomura, and Tomoki Fukai. Neural dynamics and information representation in microcircuits of motor cortex. *Frontiers in Neural Circuits*, 7:85, 2013.
- [67] Nicholas R Wall, Mauricio De La Parra, Jordan M Sorokin, Hiroki Taniguchi, Z Josh Huang, and Edward M Callaway. Brain-wide maps of synaptic input to cortical interneurons. *The Journal of Neuroscience*, 36(14):4000–4009, 2016.
- [68] Nicholas Weiler, Lydia Wood, Jianing Yu, Sara A Solla, and Gordon M G Shepherd. Top-down laminar organization of the excitatory network in motor cortex. *Nat Neurosci*, 11(3):360–366, Mar 2008.
- [69] Takayuki Yamashita, Aurélie Pala, Leticia Pedrido, Yves Kremer, Egbert Welker, and Carl CH Petersen. Membrane potential dynamics of neocortical projection neurons driving target-specific signals. *Neuron*, 80(6):1477–1490, 2013.
- [70] Naoki Yamawaki, Katharine Borges, Benjamin A Suter, Kenneth D Harris, and Gordon MG Shepherd. A genuine layer 4 in motor cortex with prototypical synaptic circuit connectivity. *Elife*, 3:e05422, 2015.

- [71] Naoki Yamawaki and Gordon M G Shepherd. Synaptic circuit organization of motor corticothalamic neurons. *The Journal of Neuroscience*, 35(5):2293–2307, 2015.
- [72] Siyu Zhang, Min Xu, Wei-Cheng Chang, Chenyan Ma, Johnny Phong Hoang Do, Daniel Jeong, Tiffany Lei, Jiang Lan Fan, and Yang Dan. Organization of long-range inputs and outputs of frontal cortex for top-down control. *Nature Neuroscience*, 2016.